Sounding rocket study of two sequential auroral poleward boundary intensifications

M. R. Mella,[1] K. A. Lynch,[1] D. L. Hampton,[2] H. Dahlgren,[3,4] P. M. Kintner,[5] M. Lessard,[6] D. Lummerzheim,[2] E. T. Lundberg,[5] M. J. Nicolls,[7] and H. C. Stenbaek-Nielsen[2]

Received 23 January 2011; revised 22 September 2011; accepted 23 September 2011; published 7 December 2011.

[1] The Cascades-2 sounding rocket was launched on 20 March 2009 at 11:04:00 UT from the Poker Flat Research Range in Alaska, and flew across a series of poleward boundary intensifications (PBIs). The rocket initially crosses a diffuse arc, then crosses the equatorward extent of one PBI (a streamer), and finally crosses the initiation of a separate PBI before entering the polar cap. Each of the crossings have fundamentally different in situ electron energy and pitch angle structure, and different ground optics images of visible aurora. It is found that the diffuse arc has a quasi-static acceleration mechanism, and the intensification at the poleward boundary has an Alfvénic acceleration mechanism. The streamer shows characteristics of both types of acceleration. PFISR data provide ionospheric context for the rocket observations. Three THEMIS satellites in close conjunction with the rocket foot point show earthward flows and slight dipolarizations in the magnetotail associated with the in situ observations of PBI activity. An important goal of the Cascades-2 study is to bring together the different observational communities (rocket, ground cameras, ground radar, satellite) with the same case study. The Cascades-2 experiment is the first sounding rocket observation of a PBI sequence, enabling a detailed investigation of the electron signatures and optical aurora associated with various stages of a PBI sequence as it evolves from an Alfvénic to a more quasi-static structure.

Citation: Mella, M. R., K. A. Lynch, D. L. Hampton, H. Dahlgren, P. M. Kintner, M. Lessard, D. Lummerzheim, E. T. Lundberg, M. J. Nicolls, and H. C. Stenbaek-Nielsen (2011), Sounding rocket study of two sequential auroral poleward boundary intensifications, *J. Geophys. Res.*, *116*, A00K18, doi:10.1029/2011JA016428.

1. Introduction

[2] The sounding rocket study, The Changing Aurora: In Situ and Camera Analysis of Dynamic Electron precipitation Structures-2 (Cascades-2), was a multipayload in situ study of the nightside lower ionosphere. The rocket was launched into the auroral zone in a fairly quiet ionosphere (Kp $\leq$ 2) with poleward boundary intensification (PBI) activity. A serendipitous conjunction with three THEMIS (Time History of Events and Macroscale Interactions during Substorms) satellites allows us to consider magnetospheric drivers to the ionospheric response [*Angelopoulos*, 2008]. In this paper we detail three specific events during the flight, two of which are classified as PBIs, and consider the large scale connection between the auroral signature in the ionosphere and the magnetospheric signatures of activity, as seen at THEMIS.

[3] A PBI, as defined by *Lyons et al.* [1999], starts at the poleward edge of the auroral oval and may pull equatorward. Observations of this type of aurora date back to the 1950s when *Davis* [1962] reported seeing north–south aligned aurora at very high latitudes, which was later defined as a PBI. Other early literature referred to these structures as north–south aligned structures or streamers [*de la Beaujardière et al.*, 1994; *Henderson et al.*, 1998]. The midpoint of our rocket flight crosses a streamer, and then goes on to cross an intensification at the poleward boundary. The electron distribution functions show fundamental differences in energy range and pitch angle structure at the two times, indicative of the changing auroral processes. For these to change as the streamer pulls equatorward indicates that the acceleration mechanism associated with a streamer, which starts as an activation at the poleward boundary, is evolving in time. A recent study by *Hull et al.* [2010] presents a similar finding with Cluster data showing that an upward current acceleration region can develop from an Alfvénic acceleration region.

[4] There are no theoretical models which explain the transition from an Alfvénic acceleration region to an upward

[1]Department of Physics and Astronomy, Dartmouth College, Hanover, New Hampshire, USA.
[2]Geophysical Institute, University of Alaska Fairbanks, Fairbanks, Alaska, USA.
[3]School of Electrical Engineering, Royal Institute of Technology, Stockholm, Sweden.
[4]Now at Center for Space Physics, Boston University, Boston, Massachusetts, USA.
[5]School of Electrical and Computer Engineering, Cornell University, Ithaca, New York, USA.
[6]Space Science Center, University of New Hampshire, Durham, New Hampshire, USA.
[7]Center for Geospace Studies, SRI International, Menlo Park, California, USA.

0148-0227/11/2011JA016428

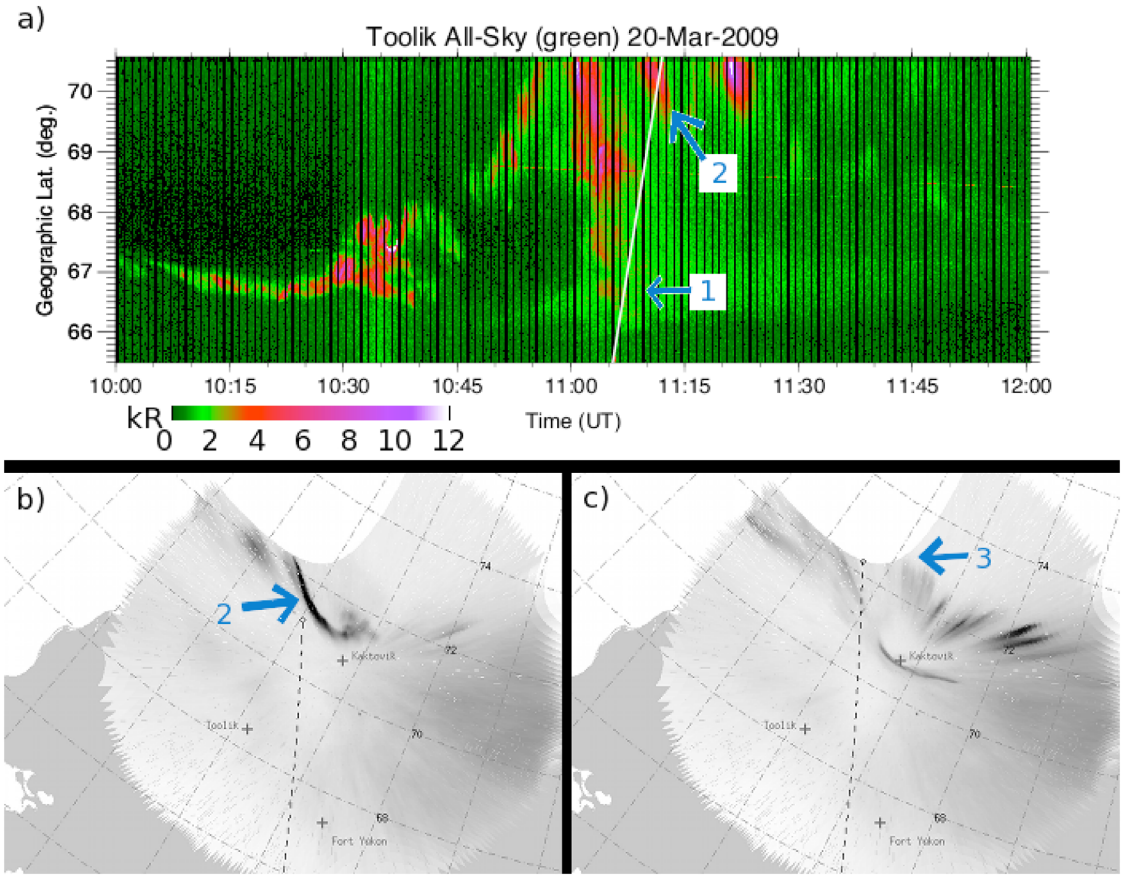

Figure 1. (a) White light keogram with the rocket trajectory overplotted and (b, c) two images from the all sky camera at Kaktovik. Auroral light associated with events 1, 2, and 3 is noted.

current acceleration region. However, it is possible for the theories explaining the different regions to fit together. *Lysak et al.* [2009] use a magnetohydrodynamic (MHD) code to show that perturbations in the magnetotail can create fast mode wavefronts which, upon encountering the plasma sheet boundary layer, convert to shear Alfvén waves and produce a field-aligned current. It is shown by *Wygant et al.* [2002] that these waves can cause particle acceleration. *Streltsov and Lotko* [2008] discuss how an Alfvén wave ponderomotive force can produce further density cavitation. In their paper they discuss evidence of auroral cavities associated with quasi-static inverted-V aurora [*Persoon et al.*, 1988; *McFadden et al.*, 1999]. The cavity associated with Alfvénic aurora is thought to develop from the auroral cavity associated with the inverted-V aurora through convection in the ionosphere [*Streltsov and Lotko*, 2008].

[5] As seen in Figure 1, along the Cascades-2 trajectory, prior to the two PBI crossings is a crossing of a broad diffuse arc at the equatorward edge of the auroral oval. Similar differences in the types of aurora are presented in a case study by *Olsson and Janhunen* [1998] and categorized by *Paschmann et al.* [2002]. The Cascades-2 flight provides the opportunity to compare and contrast these different signatures and study their evolution from one type to another, as well as to place them in a magnetospheric and ionospheric context. The Poker Flat Advanced Modular Incoherent Scatter Radar (PFISR), providing ionospheric context, was operated in a mode specifically chosen to support the Cascades-2 mission. For the magnetospheric context, the rocket trajectory foot points map to within close conjunction of three THEMIS satellites, providing the magnetotail processes and locations associated with PBIs.

[6] This paper focuses on three specific times in the rocket flight. We show that event 1 is an inverted-V, event 2 is a combination of inverted-V and Alfvénic processes, and event 3 is purely Alfvénic. We also argue that event 2 developed out of an event 3-like arc, therefore illustrating a case study where Alfvénic acceleration mechanisms do not always occur separately from quasi-static parallel potential drop acceleration mechanisms. The current understanding of auroral acceleration regions has, for the most part, kept quasi-static systems separate from time-varying systems, as noted by *Paschmann et al.* [2002, and references therein]. There are a few notable observational exceptions [e.g., *Marklund et al.*, 2001, 2004; *Aikio et al.*, 2004, 2008; *Hull et al.*, 2010], and no theoretical models of this evolution. In this paper we look at the details of the flight with an overview of the event, consider specific observations to address the goals of this study, and discuss interpretations of the data and how they relate to other studies.

2. Methodology

[7] On 20 March 2009 the sounding rocket, Cascades-2, was launched northward from Poker Flat Research Range

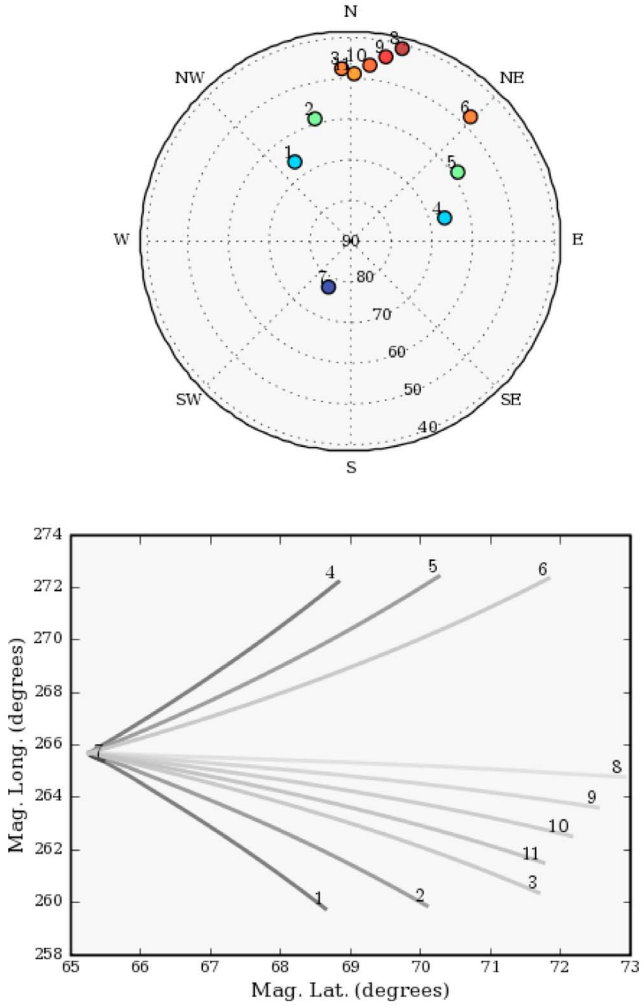

Figure 2. (top) PFISR look directions for the CASCADES-2 launch, in geographic and (bottom) geomagnetic coordinates.

(PFRR, 65.119°N, 147.432°W), Alaska at 11:04:00 UT, corresponding to 2:04 AM local time, which is roughly 23:30 MLT. The flight time was 12 min and 43 s, reaching an apogee of 564 km. The rocket consisted of five separate payloads, designed to measure particles and electric and magnetic fields at multiple points. This paper focuses on electron data acquired with a hemispherical electrostatic analyzer, sampling electrons in the range of 0–4 keV every 64 ms [*Carlson et al.*, 1982; *Arnoldy et al.*, 1999]. We also consider data from a high-speed, field-aligned electrostatic analyzer which samples electrons between 20 eV and 1 keV every 8 ms. Cascades-2 was the first flight of this new detector, named the Bagel, which was a section of a toroid, modeled after a toroidal detector used on the Phaze2 sounding rocket [*Arnoldy et al.*, 1999]. For details of this instrument, see Appendix A.

[8] In previous studies of PBIs and streamers [*Henderson et al.*, 1998; *de la Beaujardière et al.*, 1994; *Lyons et al.*, 2002], optical measurements were limited in temporal resolution to seconds or longer. For the Cascades-2 study, ground-based imagers were used to examine the optical response on timescales comparable to that of the particle detectors. Both standard Poker Flat monitoring cameras at Poker Flat (PKR, 65.119°N, 147.432°W), Kaktovik (KAK, 70.133°N, 143.633°W), and Toolik Field Station (TOO, 68.627°N, 149.594°W), and additional campaign-specific narrow-field imagers were operated at TOO and KAK during the rocket flight (Figure 1). At KAK a white-light all-sky video camera and a narrow-field intensified CCD (ICCD) camera both operated at 30 frames per second. The ICCD was filtered with a magenta filter to suppress the long-lived 557.7 and 630.0 nm emissions, collecting primarily N_2 first-positive (1P) and N_2^+ first negative emissions, both of which are prompt, allowing for accurate reproduction of auroral arc dynamics. The ICCD field of view was 20° H by 16° V. At TOO a digital all-sky camera collected images every 5 s, and a narrow-field "Guppy" CCD fitted with a 645 nm long-pass filter, collected images at 2 Hz. The Guppy CCD field of view was 24° H by 33° V.

[9] The three THEMIS [*Angelopoulos*, 2008] satellites in the far magnetotail (spacecraft A, D, & E) are located close to the neutral sheet and slightly in the premidnight sector. They are aligned in magnetic local time with the rocket, and also closely aligned to a magnetic latitude which the rocket crosses, although mapping along field lines at high latitudes introduces significant error.

[10] PFISR [*Nicolls and Heinselman*, 2007] operated for Cascades-2 in a mode designed for background diagnostics and assistance with the launch call. This mode consisted of combined long pulses for F-region densities and electric fields and a shorter, coded pulse for E-region densities, which was operated throughout the evening up until two minutes before the launch, as well as post launch (after rocket tracking had ceased). While the rocket was in-flight, PFISR operated in a reduced duty-cycle mode to minimize interference with rocket telemetry, transmitting only the shorter, coded pulses using beams pointed at azimuths close to the projected flight path. The look-directions ("beams") for the pre- and post- launch diagnostics used for this experiment are shown in Figure 2. These consisted of an up-B beam, pointed to the south (labeled "7"), 3 pairs of beams pointed northward on either side of the magnetic meridian for electric field estimation, and an additional 4 beams pointed at approximately the rocket flight path. During the launch, directions 1–7 were not utilized, and the shorter, coded pulses were transmitted in directions 8–11. In the lower panel of Figure 2 we show the magnetic latitude and longitude projections of these look directions out to 1000 km range. The pairs of beams (1–4, 2–5, and 3–6) flank the meridian for the purposes of electric field resolving. Electric fields are resolved as a function of magnetic latitude assuming spatial uniformity in the flows in longitude over the field-of-view [*Heinselman and Nicolls*, 2008].

3. Observations

[11] Figure 1a shows a visible aurora keogram from the night of launch, taken from the Toolik Lake all-sky camera along the plane of the trajectory, showing the rocket foot point between 65.49-70.57° latitude. The launch time was 11:04:00 UT. We pass through a broad diffuse arc first (event 1), at 11:07:33 UT, followed by a streamer at 11:11:45 UT (event 2), and finally pass through a rayed arc at the poleward boundary (event 3) before atmospheric reentry into the polar cap at 11:16:42 UT. We will use this

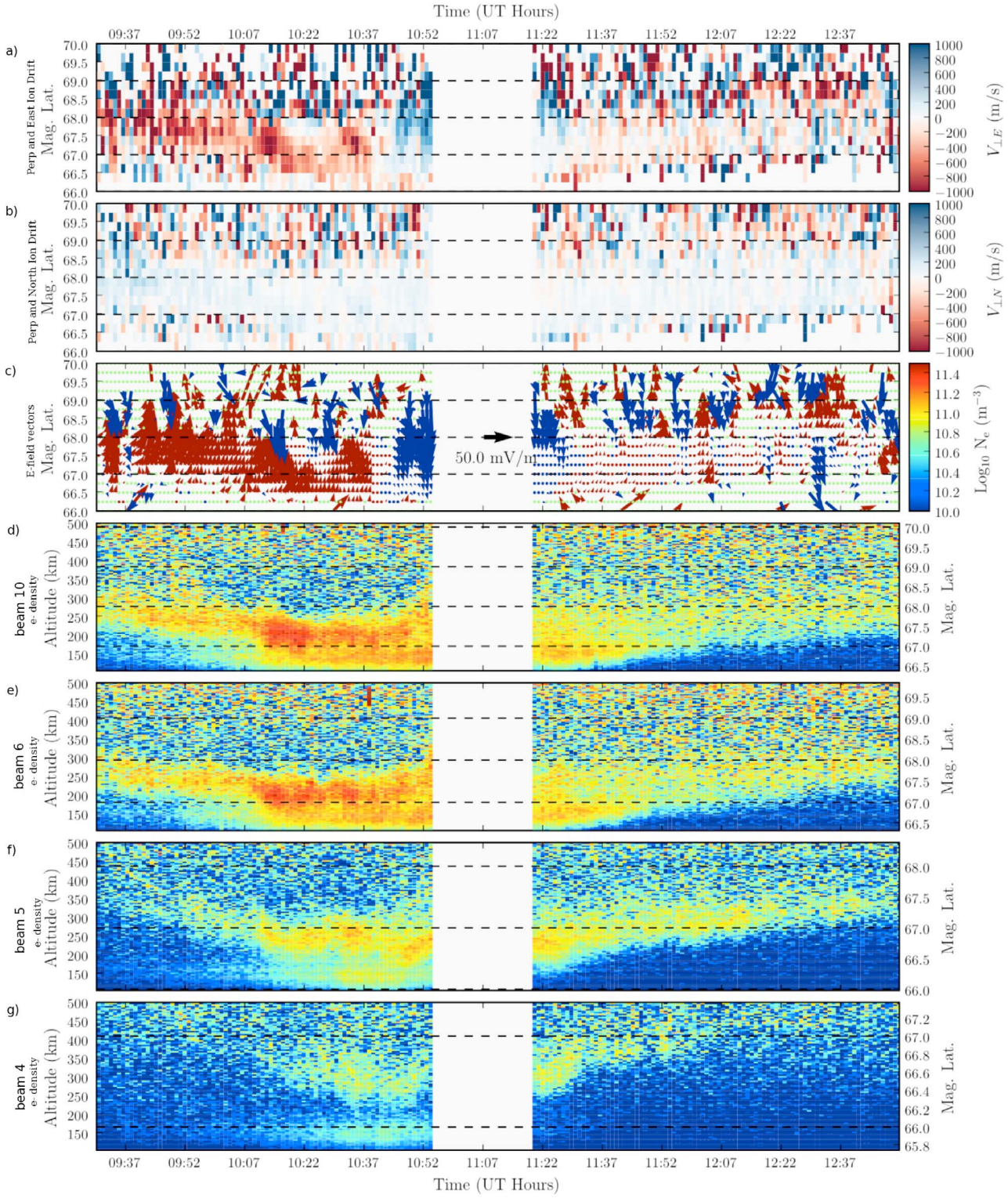

Figure 3. Summary of PFISR long-pulse observations on 03/20/2009. (a) Perpendicular and east ion drift. (b) Perpendicular and north ion drift. (c) Vector plot of electric fields, with red showing eastward fields and blue westward. (d–g) Electron densities from four look directions, from most northward-looking (lowest elevation) to least northward looking (highest elevation) (beams 10, 6, 5, 4). Dashed horizontal lines in each plot correspond to lines of magnetic latitude.

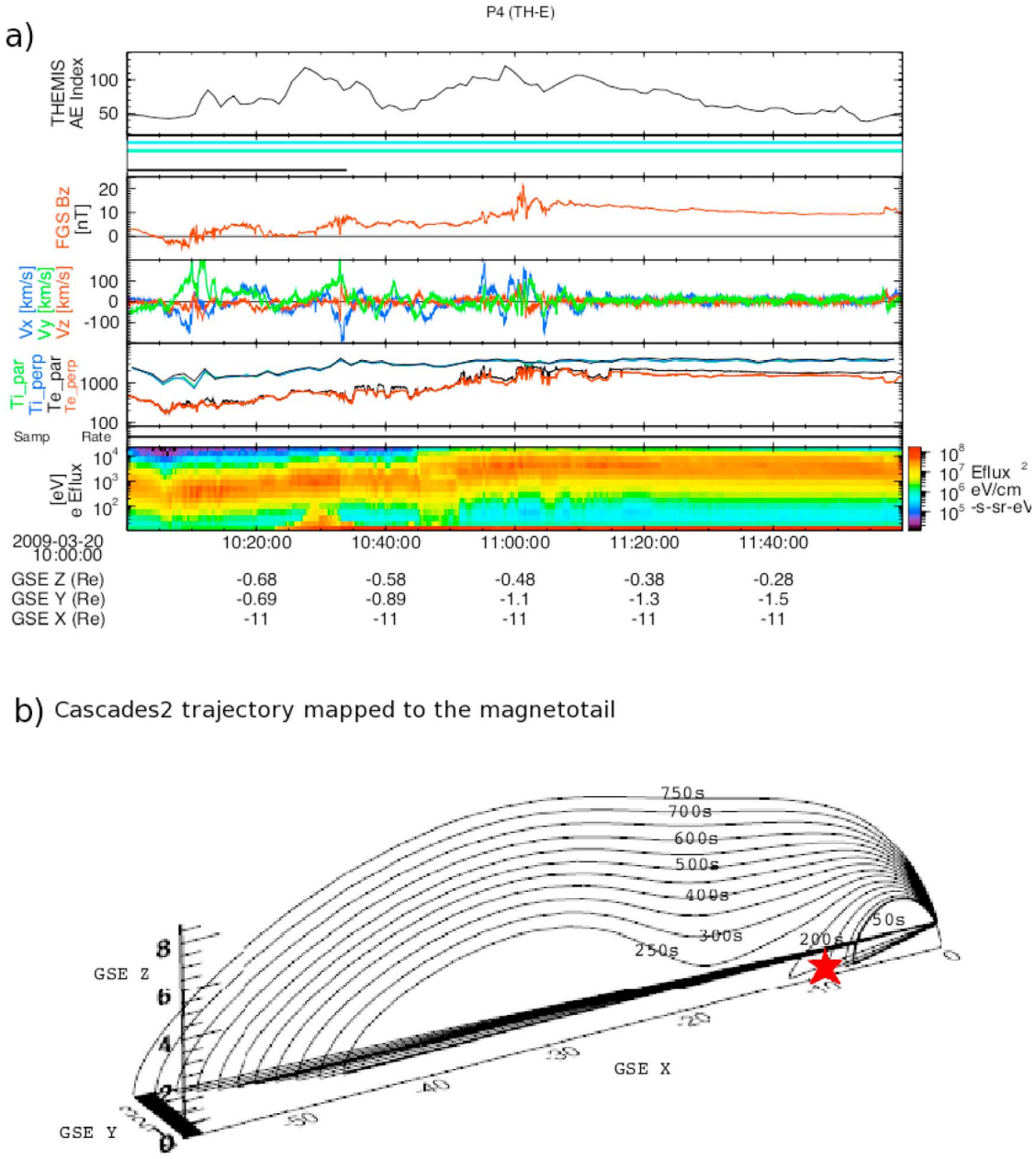

Figure 4. (a) An overview of THEMIS data from the night of launch. (top to bottom) Pseudo-AE index generated from the ground based observatories. The region of interest, indicating TH-E is in the Average Plasma Sheet region, as well as in the Radial Distance Region 1, and, prior to 10:34 UT, in the Earth's shadow. The z-component of the magnetic field. The vector components of the plasma flows. The perpendicular and parallel ion and electron temperatures. The data collection mode, which is the fast survey mode (bar). The electrostatic analyzer electron energy flux spectral plot. (b) A mapping of the rocket foot points to the plasma sheet. Approximate location of THEMIS A, D, and E is marked with a red star.

event 1, 2, 3 terminology throughout the paper. The poleward boundary was determined primarily by the abrupt end of in situ electrons and high energy ions, and verified by the all sky cameras. Figure 1b shows two images from the Kaktovik ASC, highlighting the tall, rayed curtain (event 3) at the poleward boundary which is out of the field of view of the Toolik keogram.

[12] These poleward boundary intensifications (events 2 and 3) were well to the north of PFISR's field-of-view. Therefore, the PFISR data taken during the launch, optimized for E- region measurements, did not observe the characteristics of the PBIs being measured in situ by the rocket. The pre- and post-launch data, however, are useful from a background and diagnostic perspective. These PFISR measurements are summarized in Figure 3, with the data taken during the time of flight in the reduced duty-cycle excluded, since PFISR's field of view then only overlapped with our event 1. The top two panels of Figure 3 show the

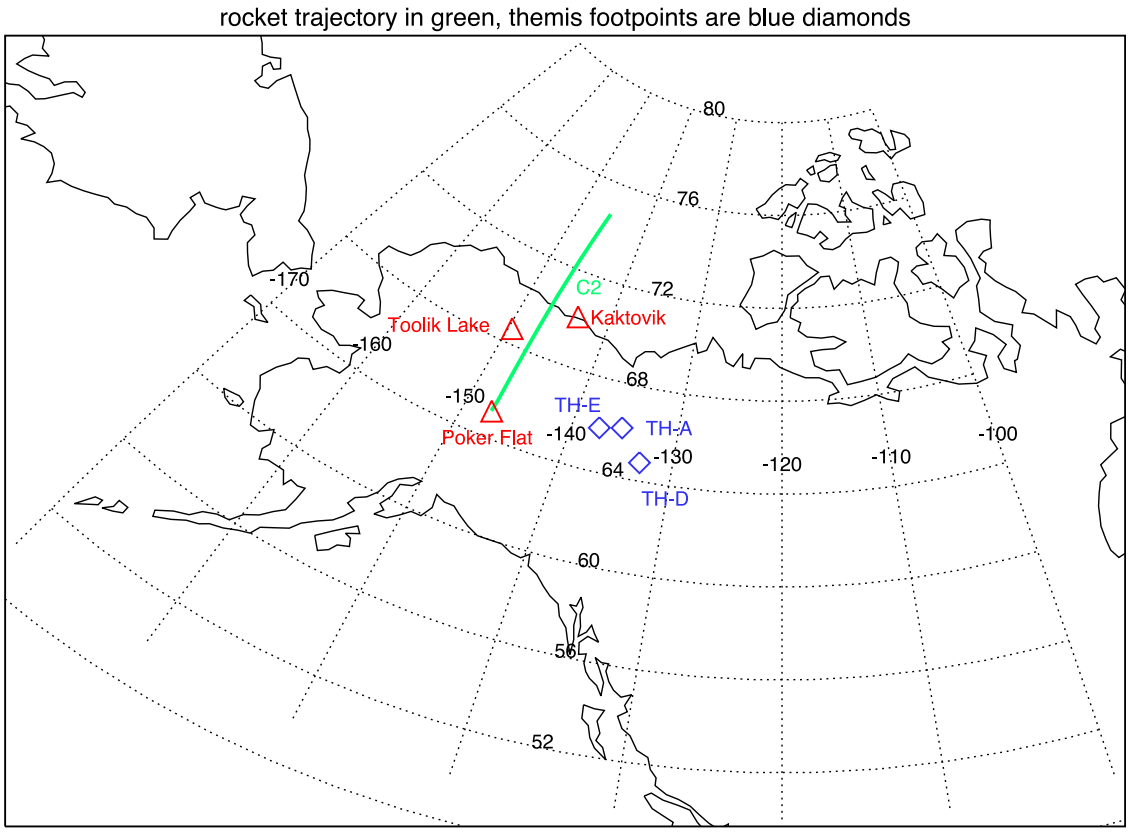

Figure 5. A map of Alaska showing the Cascades-2 rocket trajectory (green trace); the location of the ionospheric foot points of THEMIS A, D, and E (blue diamonds); and the three ground stations (red triangles).

perpendicular east and north **E** × **B** flows ($V_{\perp E}$ and $V_{\perp N}$). The data gap from ~11-11:20 UT corresponds to the flight time. The third panel shows vector plots of the flows converted to electric fields. The observed latitudinal gradients in the ionospheric electric fields are associated with auroral arcs and electron precipitation. These, in turn, (for example, especially on the poleward boundary of the flow channel) are often associated with converging/diverging electric fields, meridional Pedersen currents, and likely field-aligned currents.

[13] The measurements are characterized by strong westward flows (corresponding to an eastward electrojet, consistent with magnetometer measurements) before 10:40 UT, reaching over 1000 m/s (~50 mV/m northward electric field). The region of enhanced westward flows is confined within a ~1-1.5° latitude channel that moves southward in time. Throughout the Cascades-2 field campaign (February - March, 2009) this equatorward motion of strong westward flows proved to be a reliable observational precursor to auroral activity of both substorm and PBI related events. At about 10:40 UT, the flows suddenly reverse to the east and remain strong and eastward through the launch period.

[14] Electron densities are plotted in the lower panels of Figure 3 for four representative beams: from north to south, beam 10, 6, 5 and 4. Note that the observed ionization appeared to be quite uniform in longitude. The altitude and magnetic latitude of the measurements are indicated on the left and right y-axes, respectively. The densities show a clear and strong latitudinal gradient. Toward the south, two distinct regions of enhanced ionization are observed: one at lower altitudes (confined in general to 100–150 km, as identified in the E-region shorter-pulse data, not shown) and one in the F-region likely associated with soft electron precipitation. At the higher latitudes, the two populations blend in together. In terms of time variation, the region of softer precipitation appears to penetrate downward and/or southward in time. Due to the similarity in the electric field observations, and the fact that the ionization appears later in time in the beams toward the south, the apparent motion is likely true latitudinal penetration. This would imply that the electron plasma sheet is moving tailward, and the magnetic field of the earth is becoming less-dipolar with a more stretched tail, as magnetic local time progresses.

[15] The distinct region of lower-altitude ionization observed south of the soft precipitation is likely due to proton precipitation, which is a common source of ionization at the equatorward edge of the diffuse aurora in the evening sector [*Robinson and Vondrak*, 1985; *Zou et al.*, 2009]. The PFISR flow region signature moves equatorward as the electron plasma sheet precipitation (PFISR electron density) penetrates equatorward, which, in general, is associated with substorm growth phase; however, this auroral activity did not develop into a large substorm, but rather, into a series of poleward boundary intensifications.

[16] Figure 4 is an overview plot of data from THEMIS-E. This plot shows alternating earthward and tailward plasma

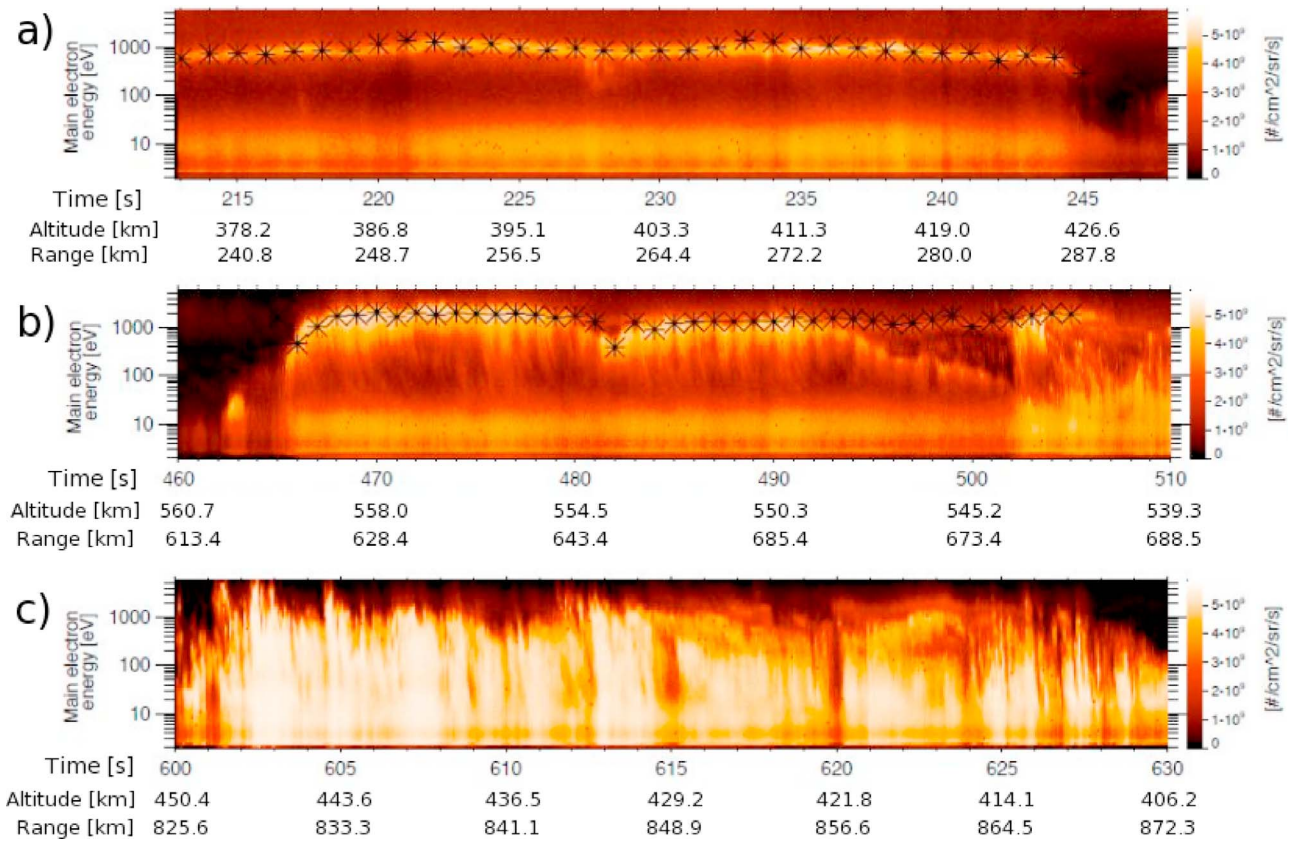

Figure 6. In situ spectrograms of electron energy from the main payload electron electrostatic analyzer, separated into (a) event 1, (b) event 2, and (c) event 3 (plotted in seconds from launch time), to highlight the differences of each event.

flows occurring between 10:10 UT and 11:30 UT. Just prior to the time of the rocket flight, between 10:55 UT and 11:04 UT, there are strong earthward plasma flows. There is also a small dipolarization at 11:00 UT. THEMIS mapped to a geographic latitude of 66° and longitude of −138° in the ionosphere, which is in very close conjunction with our rocket foot point (which flew from −147.5 to −145.5° longitude and from 65.1 to 74.9° latitude). Due to the limitations of mapping the THEMIS foot point from the magnetosphere to the ionosphere, these data are presented to give an idea of the activity in the magnetotail that is in close (but not exact) conjunction with the rocket, for a broader understanding of the large scale activity. While one-to-one correlations are not being made, the data provide the magnetospheric context for the rocket data. Figure 4b shows the mapping of the rocket foot points to the magnetotail using the 2004 Tsyganenko model [*Tsyganenko and Sitnov*, 2005]. The foot point moves from the near-Earth plasma sheet to the distant magnetotail as the rocket flies northward with time.

[17] A map of Alaska is shown in Figure 5, which includes a green trace for the Cascades-2 rocket trajectory. Also plotted are the THEMIS ionospheric foot points using the same model as above, as well as the locations of the ground stations used for optical studies in conjunction with this rocket study.

[18] Figures 6 and 7 present the in situ rocket data showing the electron differential energy flux spectrogram. Figure 6 is from the hemispherical electrostatic analyzer, with each panel showing a different time of flight, corresponding to events 1, 2, and 3. Figure 7 is a plot of electron data from the Bagel detector for shorter time periods during events 2 and 3, to show the time dispersed electrons present during each of these events, which are not present during event 1. Figure 8 presents the pitch angle distribution for events 1, 2, and 3.

[19] Event 1 shows an inverted-V signature at higher energies (0.5-1 keV), with an isotropic pitch angle distribution with a loss cone. In event 2 the flux enhancement is now more widely spread in energy (0.1-3 keV), showing a clear distinction between events 1 and 2. The pitch angle distribution shows an even stronger difference with the addition of a very field aligned population, as seen at 474 s time of flight, that is never more than 20 degrees wide. During event 2 there is both the isotropic with loss cone population, and also the field-aligned population. In the energy spectrogram (Figure 6) the two separate populations can be distinguished between 495 s and 502 s time of flight, when the two populations are spaced in energy. The approximate 1 s modulation in the high energy population is an artifact of payload spin. Event 3 takes place at the end of flight, just before entry into the polar cap. The electron energy spectra here are very broad, and have distinct dispersion signatures as seen in Figure 7. Here the pitch angle image is field-aligned (Figure 8), but slightly less narrow than event 2, with a higher perpendicular electron temperature. Also seen occasionally is an upgoing electron population, which can be seen in Figure 8, at 602 s time of flight, ranging in energy from 10 to 900 eV at 180 degrees. Notably the more

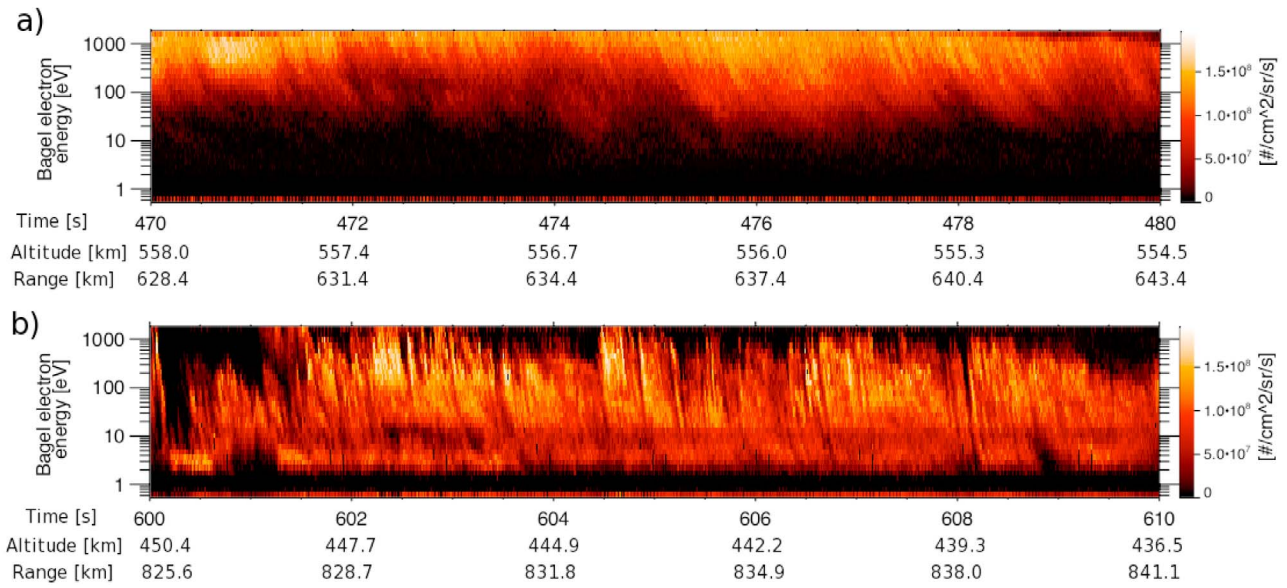

Figure 7. In situ spectrograms of electron energy from the main payload, high-speed, field-aligned detector (Bagel), separated into two ten second time periods (plotted in seconds from launch time) from events (a) 2 and (b) 3, to highlight the time-dispersed electrons of each event.

isotropic population is missing in event 3. We discuss specifics of these source temperatures in section 4.3.

[20] In situ DC (0–1 kHz) electric field data are shown in Figure 9, which are despun into a magnetic Vertical-East-North coordinate system with the x-axis aligned to B_0, the z-axis pointed toward the magnetic pole (meridional), and the y-axis completing the right-handed triad (see E. T. Lundberg et al., Multi-payload measurement of transverse velocity shears in the topside ionosphere, submitted to *Geophysical Research Letters*, 2011). At the time of event 2, no strong low-frequency electric field fluctuations are seen, whereas at the time of event 3 (after 580 s flight time) very strong low-field electric field fluctuations are measured on the rocket.

[21] Figure 10 presents in situ data of the event 3 electron pitch angle structure as a function of time, for energies summed between 15 eV and 5.8 keV. It shows a heated, field-aligned population at the time of event 3. There is also an enhanced upgoing population seen at flight times of 602.5-603.5 s, 604.5 s, and 607 s, appearing in the bin just below the 180 degree tick mark. Overplotted is the in situ ambient thermal electron temperature (right axis) as measured by the Electron Retarding Potential Analyzer (ERPA)

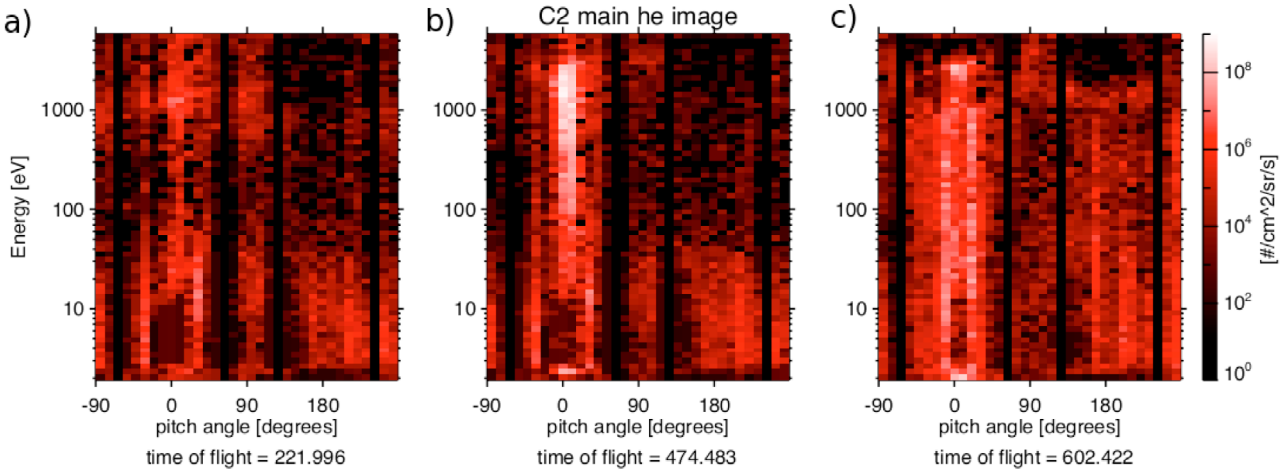

Figure 8. In situ energy-pitch images, separated into (a) event 1, (b) event 2, and (c) event 3, to highlight the differences of each event. The vertical black stripes in each image represent mechanical blind spots of the detector. Note that in each image, the thermal electrons (2.5 eV to 10 eV) ranging from ±20 degrees from the down-going direction (0 degrees) are undergoing a $\mathbf{v} \times \mathbf{B}$ drift within the detector, which is erroneously showing a "hole" in the data in that range.

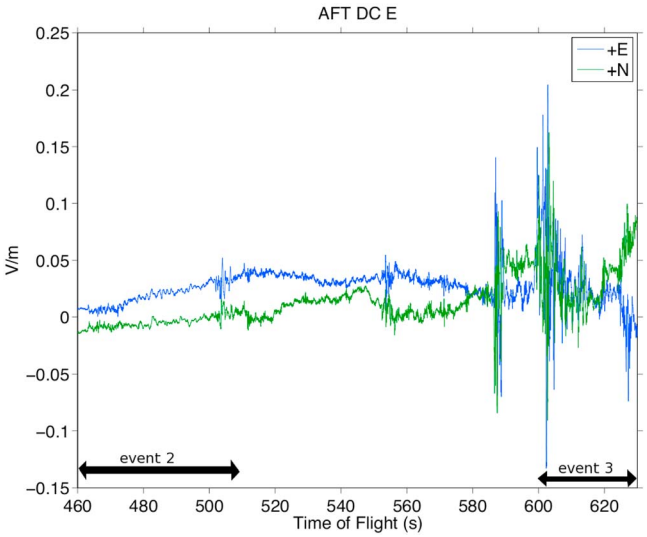

Figure 9. In situ DC electric field measurements from the Aft subpayload, from 460–630 s time of flight, which covers the span of events 2 and 3.

detector [*Frederick-Frost et al.*, 2007]. Figure 10 also illustrates the different widths of the field-aligned population which corresponds to the ionospheric electron temperature. Before 602 s, as in event 2, the source population is a cold, ionospheric population. At this time, the field aligned population is very narrow, less than 10 degrees in pitch angle. After 602 s, and persistent through the remainder of event 3, the source population is a heated, ionospheric population. *Watt et al.* [2004] have shown that Alfvén waves can accelerate cold ambient thermal electron populations to energies sufficient to power visible aurora. Here the electrons are still field-aligned, but not quite as narrow in pitch angle.

4. Discussion

[22] In the following sections we will discuss the three main events in detail, first considering the in situ rocket data. Then we compare the in situ rocket data to ground optical data. Finally we consider THEMIS data to make the comparison between the magnetospheric and ionospheric signatures observed.

4.1. Event 1, in Situ

[23] Event 1 begins at 212 s time of flight, corresponding to 11:07:32 UT (Figures 6a and 8a). The associated visible aurora observed with multiple ground cameras and spectrographs is a broad, diffuse, stable arc that remains unchanged at the equatorward edge of the auroral oval from the time of flight until several hours later. The in situ electron flux enhancement is at least 50 km wide, as seen in the range extent of Figure 6a. The approximate 50 km arc width is also seen in the camera data. Leading up to 10:30 UT there was one visible faint arc (less than 2 kR) in the sky that gradually pulled equatorward. Concurrently, westward flows were observed by PFISR (not shown) to move equatorward. Between 10:30 UT and 11:00 UT an auroral activation occurs, as seen in Figure 1a by an arc brightening, breaking up, and moving poleward. At 11:00 UT THEMIS observes a dipolarization in the magnetotail near 10 Re. After this activity, there is a double oval configuration in the ionosphere [*Elphinstone et al.*, 1995], as observed by ground cameras. Our event 1 is the crossing of the arc that remains from the original arc present before the aurora activation.

[24] The in situ data presented in Figure 6a show a typical inverted-V signature in the electron spectrogram. It is very narrow in energy, with enhanced fluxes ranging between 500–2000 eV. The arc has lower energies on the edges, corresponding to a spatial structure that the rocket is moving through, as opposed to a structure changing in time. In the pitch-energy image the electron population is seen to be isotropic with a loss cone. This electron population is caused either by a small potential drop located high on the field line, according to the definition of an inverted-V, or by an unaccelerated population that is precipitating into the ionosphere, as the peak energy flux is near twice the source electron temperature. The star points overplotted on the spectrograms for this event as well as event 2 (Figure 6b) are at twice the calculated value of the source electron temperature. This is done by assuming the measured in situ population is a Maxwellian, and then calculating the temperature by taking the derivative with respect to energy of the natural log of the distribution function. As the expected peak in differential energy flux should be at twice the source temperature plus any acceleration potential greater than twice the temperature, the matching of these points with the peak flux means the acceleration potential is either zero or smaller than twice the temperature. This source temperature calculation indicates the observed electron spectrogram signature is well modeled by a roughly 450 eV source temperature precipitating population with minimal acceleration.

[25] This event fits both the visible and electron spectrogram signature definitions of a typical inverted-V with a minimally accelerated Maxwellian distribution [*Evans*, 1974]. If the population is unaccelerated or has a very small acceleration, the variability seen in the electron spectrogram could come from a source of varying temperature. It could also be a

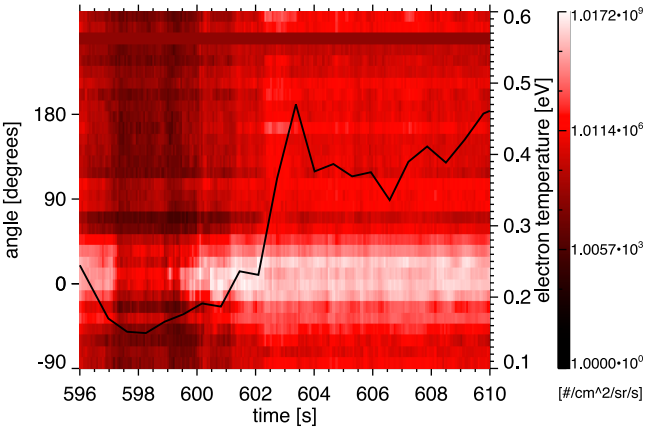

Figure 10. Variable pitch angle structure of the electron activity in event 3, with a trace of the electron temperature overplotted, shows the electron heating associated with event 3. Note the width of the field-aligned population is broader when the electron temperature is higher. Prior to event 3, the electron temperature is much colder, and the field-aligned population is more narrow.

signature of an inverted-V far above the observation point which, upon reaching the observation point, has become somewhat thermalized such that the observed source temperature is a combination of the original thermal energy of the source plus a contribution from the inverted-V potential drop.

4.2. Event 2, in Situ

[26] Event 2 occurs in the middle of the flight, beginning at 465 s time of flight, or 11:11:45 UT (Figures 6b, 7a, and 8b). At 11:10 UT (360 s time of flight) a visible rayed arc was aligned magnetic E-W at 72° north geomagnetic, along the poleward boundary of the auroral oval. This arc brightened to ~2-4 kR and expanded equatorward as a streamer until it reached 71° north geomagnetic by 11:12 UT, over an approximately 5° longitudinal range. The rocket crosses this streamer after the arc at the poleward boundary has extended equatorward, away from the poleward boundary, as seen in Figure 1b. The arc moves quickly through the sky, on the order of 10 km/s, but retains its shape as one connected arc. Examining only the in situ electron energy spectrogram in Figure 6b would lead one prematurely to define it as an inverted-V arc, as the energy of enhanced fluxes is restricted to a band ranging from 0.1–3 keV. However, a narrow energy range is only part of the definition of an inverted-V, and the electron pitch angle structure must be examined. The pitch-energy image in Figure 8b shows there to be two populations: a narrow, field-aligned beam from 0.1–3 keV, and an isotropic population ranging from 1–3 keV which is similar to that of event 1. The field-aligned population has a $T_\perp$ of less than 1 eV, consistent with an ionospheric source. The isotropic population, as in event 1, is well modeled as a weakly accelerated Maxwellian with a source temperature of roughly 550 eV, as indicated by the overplotted points in Figure 6b.

[27] Event 2 is not solely an inverted-V but rather a mixture of precipitation from a hot plasma sheet source and a cold ionospheric source. In the higher time resolution electron detector, velocity dispersion signatures in the energy spectrogram of the field-aligned population are seen, indicating a good fit with a localized acceleration source 500–900 km up the field line from the rocket, corresponding to an altitude of 1050–1450 km. This is consistent with a wave-accelerated local population being accelerated to high energies, on top of the event-1-like precipitating isotropic population. Note, however, that in contrast to event 3, no strong Alfvénic E-fields (Figure 9) are seen at the rocket altitudes in event 2.

[28] Typically, narrowly field-aligned but broad-energy populations such as are seen in event 2 are interpreted as Alfvénic acceleration of the ambient cold ionosphere. It is also possible, since this arc structure is moving rapidly across the sky, that a quasi-static potential drop that is extended in altitude, is accelerating the ambient cold ionosphere downward. However, such dispersion signatures as are seen in event 2 (Figure 7), as well as the apparent cold source, both seem to indicate a fairly low altitude for this interaction (1050–1450 km), favoring the Alfvénic interpretation. This is the in situ electron signature of an equatorward-extending PBI, originally termed streamer. Figure 1a shows the difference in the visible aurora between events 1 and 2, while Figure 6 shows the difference in the electron energy spectra, and Figure 8 shows the difference in pitch angle structures. The field-aligned population here has a pitch angle not more than 20 degrees wide, consistent with a cold (T_e < 1 eV) ionospheric source.

4.3. Event 3, in Situ

[29] Event 3 occurs at the end of flight, beginning at 600 s time of flight, which is 11:14:00 UT (Figures 6c, 7b, and 8c). The ground cameras observe Alfvénic aurora at the poleward boundary as seen in Figure 1c. Observations of Alfvén waves at the boundary layer from the Polar spacecraft have been reported by *Wygant et al.* [2000] and *Keiling et al.* [2003], as well as from FAST by *Chaston et al.* [2003, 2006], and on rockets by *Lynch et al.* [1996]. Tall rays extending from 100–300 km altitude, joined in a rayed arc (~2-3 kR), can be seen with the narrow field cameras located at the field stations in the north of Alaska (not shown). The visible signatures are very active and dynamic, with swirling rays moving along the curtain at 8 km/s or faster, some in the geomagnetic east direction and some in the geomagnetic west direction, in a limited latitudinal band of one degree. *Ivchenko et al.* [2005] report observations relating thin rayed aurora to Alfvénic acceleration.

[30] The in situ electron energy distribution shows electrons with very broad T-parallel, ranging from 0–1.5 keV (as seen by the energy ranging from 0–3 keV in Figure 6c), but a very cold T-perp (as seen by the narrow field-aligned pitch angle in Figures 8 and 10), indicating an ionospheric source. Dispersion signatures in the energy spectrogram (see Figure 7b) indicate a source altitude between 100 km and 600 km above the rocket, corresponding to an acceleration altitude of 500 km to 1000 km. An electron population moving up the field line is also observed, as seen in Figure 8, indicating a backwash of the precipitating population due to the thermal velocity being greater than the drift velocity [*Carlson et al.*, 1998]. When the upgoing population is observed, the precipitating population is suppressed (see Figure 10), perhaps indicative of a varying bulk drift velocity. The precipitating electron population is a cold ionospheric population being locally heated as seen by the black line of low electron temperatures in Figure 10. Studies have shown the aurora at the poleward edge of the auroral oval to be Alfvénic [*Paschmann et al.*, 2002], which we can confidently say includes the PBIs of this study, as the rocket observes strong DC E-field fluctuations at the time of event 3 (Figure 9) (Lundberg et al., submitted manuscript, 2011).

4.4. Arc Altitude Profiles and Electron Energy Spectra: Comparison Between Ground Cameras and in Situ

[31] Once visible arc positions are established using triangulation from the TOO Guppy camera and KAK all-sky, altitude profiles of the two arcs can be compared to one another and to modeled profiles [*Lummerzheim and Lilensten*, 1994] as shown in Figure 11. Modeled N_2 first-positive (N_2-1P) emission rates were calculated for a set of Maxwellian distributions with peak energies of 100, 200, 400, 700, 1000, and 2000 eV. These are shown for distributions normalized to 1 mW/m^2.The altitude profile for the event 2 arc has a much narrower profile in altitude extent than the profile of the event 3 arc. The visible signature of the event 2 arc is well modeled with a 2 keV Maxwellian distribution. The excess in the measured profile above 140 km may be either a contribution from lower energy

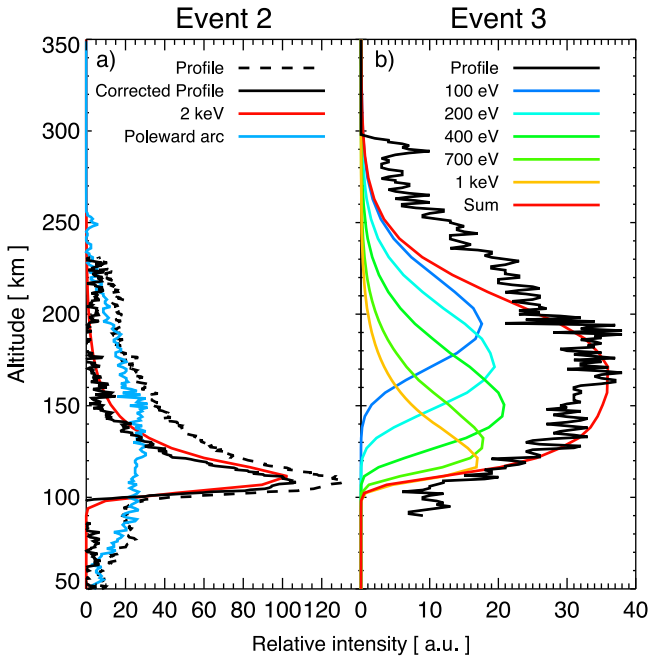

Figure 11. Light intensity profiles for events (a) 2 and (b) 3, as measured by ground cameras are plotted in black. Also plotted are calculated emission rate profiles for N2 and N2+ emissions for Maxwellian distributions with several energies. In Figure 11b these profiles are summed (red line) in order to find a reasonable match to the measured profile.

particles, or background contamination from the event 3 arc. Due to the observing geometry from Toolik (see Figure 5), the event 2 arc profile is contaminated by emissions from the rayed arc to the north. The rayed arc is comprised of low-energy electrons which are producing very dim light which is hard to see in Figure 1b, but if you imagine looking north with a narrow-field camera located to the south of Figure 1c, both the arc overhead, and the rayed arc to the north, would be overlapped. The event 3 arc is not well modeled by a single Maxwellian distribution, but when the profiles from several distributions are summed, the resulting profile has a broader height distribution and more closely matches the measured profile.

[32] The discrete and rayed arcs associated with the particle events measured by the rocket payload at 11:11:45 (event 2) and 11:14:30 UT (event 3) showed significantly different emission profiles in altitude. Altitude profiles collected by the Guppy camera at TOO are shown in Figure 11, with the event 2 arc profile taken at T + 450 s (11:11:30 UT) and the profile of the rayed arc (event 3) taken at T + 603 s (11:14:03 UT). The blue line in Figure 11a is the profile from the poleward rayed arc at T + 603 s adjusted in elevation due to the greater range. This profile is representative of the background contamination and is subtracted from the event 2 arc profile to give the corrected profile. The discrete arc profile in Figure 11a shows a sharp peak in emission near 110 km. Emission rate profiles for N_2 1P emissions were calculated for Maxwellian electron distributions with several characteristic energies using a collisional transport code [*Lummerzheim and Lilensten*, 1994]. The corrected profile is well matched by the transport code profile for a Maxwellian distribution with characteristic energy of 2 keV. In contrast, the profile of the event 3 rayed arc peaks at 170 km, but it is not sharply peaked, as seen in Figure 11b.The low altitude boundary of 105 km indicates that electrons with energies on the order of 1 keV are present. Yet the intensity of the profile at 200 km is comparable to that at 110 km. The profile cannot be matched by any single intensity profile produced by the transport code using a single energy Maxwellian distribution. Only by combining multiple profiles can a reasonable match to the measured profile be reconstructed, such as shown in Figure 11b. Again, this matches the in situ event 3 measurements which show a constant flux from low energies to a cutoff of energy of around 1 keV above which the flux is negligible. This spectrum is consistent with previous studies that concluded that such spectra are a result of acceleration by dispersive Alfvén waves [e.g., *Chaston et al.*, 2003].

[33] Altitude profiles of ionization rates can also be modeled from the in situ electron spectra throughout the flight. Figure 12 shows a profile constructed in this way from event 2 (first panel) and two profiles from event 3 (second and third panels). The final constructed event 3 profile looks very similar to the optically observed profile of visible light intensity from event 3 as shown in Figure 11. However, the profile from event 2 does not look like a single Maxwellian distribution, as was found by examining only the ground camera data. This may be because the in situ and camera observations may not be exactly common volume in this very structured event.

[34] Using the same collisional transport code [*Lummerzheim and Lilensten*, 1994], we can calculate N_2 ionization rate profiles expected from electron spectra measured on the rocket. A calculated profile typical for event 2 is shown in Figure 12a. This profile can be directly compared to that of Figure 11a, which shows the light intensity of the event 2 arc, as measured from a ground camera. The most obvious difference is the presence of a small bump at a higher altitude than the peak, in the ionization rate profile, which is not present in the light intensity profile. The light intensity profile simply matches that of a mono-energetic Maxwellian population. The auroral light visible from the ground is dominated by the high energy population, without giving any information about lower energy electrons. There is an inconsistency between the two calculated profiles in the lower energy (higher altitude) region, where no light intensity is seen, despite a small enhancement in emission rate. Also plotted are calculated profiles typical of event 3, in Figures 12b and 12c. Note the similarities in ionization rates from the electron spectra of event 2 and event 3. However, for event 3, Figure 12b, the higher altitude peak (corresponding to lower energy electrons) is not quite as strong as the low altitude peak. And for a slightly different time in event 3, Figure 12c, the peak in ionization rate is spread over a wide range of energies. This profile actually compares quite nicely in nature to the event 3 light intensity profile measured by the ground cameras. These further calculations of ionization rate altitude profiles from in situ electron spectra confirm the results found with the ground camera data, namely, that the acceleration mechanism is Alfvénic. The ionization rate altitude profile calculations of event 2 have a slightly different result than that from the ground camera results. We have shown that the

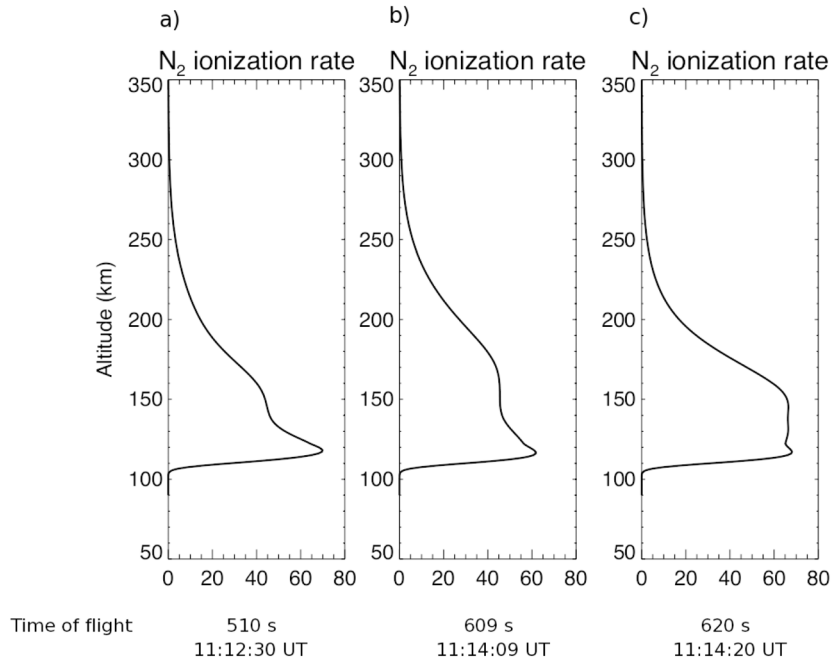

Figure 12. Calculated ionization rate altitude profiles from in situ electron spectra. (a) A profile from the time of event 2 and (b, c) profiles taken from event 3.

measured electron spectra in event 2 do not result in an ionization rate that is a single energy Maxwellian distribution. The altitude profile is dominated by a Maxwellian distribution, but there is a distinct signature at a slightly higher altitude, which actually resembles the altitude profile from event 3.

4.5. THEMIS View of Cascades-2 Events: Comparison Between Magnetosphere and Ionosphere

[35] The rocket flight was a half hour pre-midnight in magnetic local time. The trajectory maps, using TS04+IGRF, from −8 Re to −50 Re downtail in the equatorial plane. The modeling at high latitudes is often inaccurate and must be used only for a qualitative understanding of the magnetospheric configuration at the time. Three THEMIS satellites are at approximately the same magnetic local time, remaining at about −10 Re downtail throughout the rocket flight. *Zesta et al.* [2006] map PBIs to −30 Re or further, which corresponds to the mapping of the rocket foot point when it crosses the PBIs.

[36] Using THEMIS together with Cascades-2 and also PFISR, we can analyze the sequence of the large scale events. Figure 1 shows ground camera data which show the aurora brightening at 10:30 UT (event 1 is the remnant of this). This occurs prior to the only observed near Earth dipolarization at THEMIS-E at 11:00 UT as seen in Figure 4. It is possible that an earlier dipolarization occurred in the tail where THEMIS was not located. From the data available, the observations show auroral brightening occurring before the near Earth dipolarization, which fits neither the inside-out nor the outside-in model of a substorm [*Lui*, 2001]. This event is consistent with studies done by *Keiling et al.* [2008], which have reconnection in the far magnetotail occurring first, followed by auroral brightening in the ionosphere, followed by a near Earth dipolarization. There are no THEMIS satellites in the distant magnetotail at the time of our event, but we can infer when the reconnection (related to the observed dipolarization) is occurring by looking at the time of the observed earthward plasma flows which are generated at the reconnection point. On the night of our launch the alternating earthward and tailward plasma flows at THEMIS-E between 10:10 UT and 11:00 UT (see Figure 4a) are indicative of those at all three THEMIS satellites in the far magnetotail, which begin before the aurora brightens and continue until the dipolarization. Between 10:55 UT and 11:00 UT the plasma flows are strongly in the earthward direction. At 10:00 UT there was likely an enhancement of localized reconnection in the far magnetotail. For our event the aurora continues to be bright beyond times when flows are seen. It is possible that no more plasma flows are seen because THEMIS is moving closer to dusk and out of the plasma sheet. It is also possible that the magnetotail is no longer in a very stretched configuration with bursty reconnection causing plasma flows, but has settled into a dipole-like configuration, which is why the dipolarization is seen at THEMIS-E at the time when the plasma flows stop. Since the aurora continues to be bright until 11:30 UT, it is not likely that the reconnection has stopped. As the rocket approaches the poleward boundary of the auroral oval at 11:14 UT, its foot point maps to beyond −40 Re. This poleward boundary region is where the rocket sees both DC electric field fluctuations with peak-to-peak intensities greater than 300 mV/m and electrons that are very broad in energy spectrum, indicative of Alfvénic aurora. This lends further support to the idea that reconnection at a distant X-point is causing Alfvén waves to travel along the last closed field line down to the ionosphere [*Hasegawa*, 1976]. In the ground cameras at Kaktovik, we can see the tall, rayed aurora before 10 UT, which is before the THEMIS satellites observe plasma

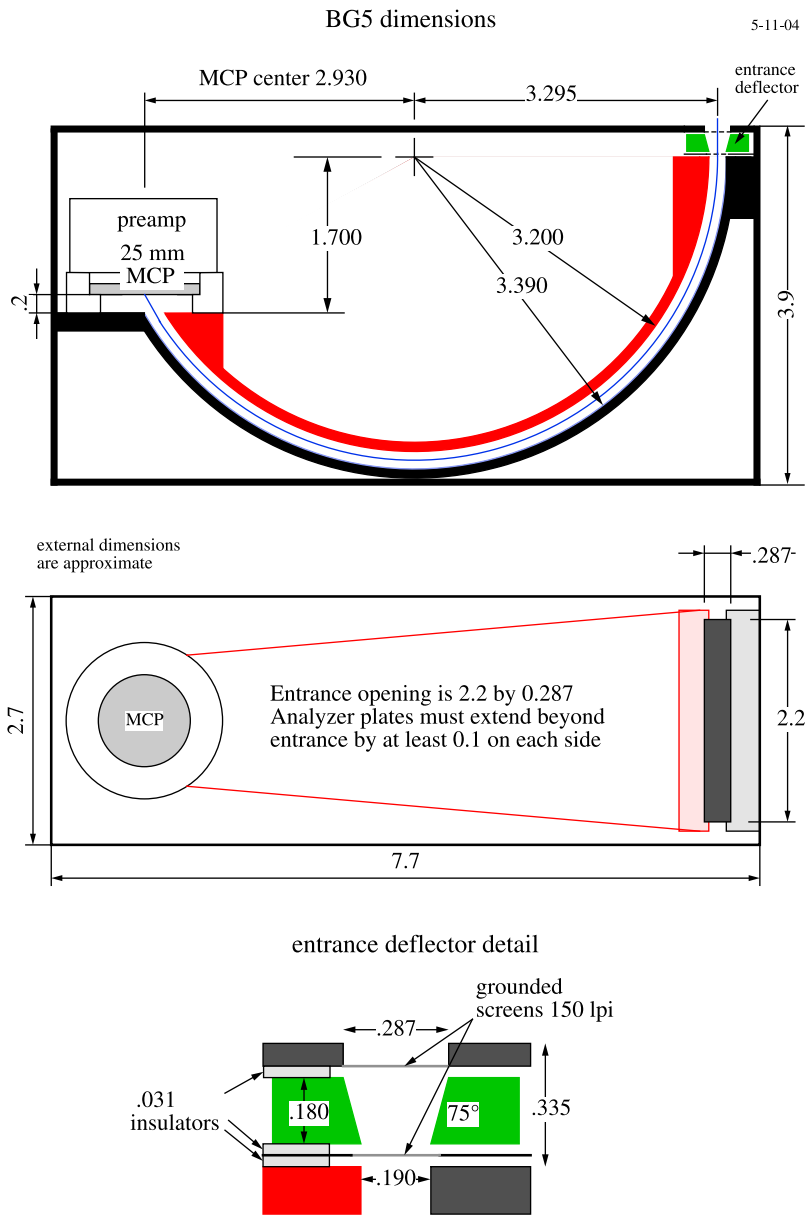

Figure A1. Dimensions of the Bagel detector, designed by Mark Widholm, EOS, UNH.

flows. This aurora is of the type which the in situ data from our flight shows to be Alfvénic activity.

[37] A recent study by *Kepko et al.* [2009] shows an equatorward moving diffuse auroral patch to be associated with earthward plasma flows in the magnetotail. The observed plasma flows at THEMIS are between 100–300 km/s, which is similar to our event. *Kepko et al.* [2009] calculate the flow burst to originate at −28 RE, corresponding to a velocity of 300 km/s traveling for 6 min (which is the amount of time prior to substorm onset that the diffuse auroral patch is observed to be moving equatorward). The diffuse auroral patch is said to be moving slowly, which is correlated with the earthward motion of the plasma flow in the magnetotail. In our rocket study, we try to similarly relate the equatorward motion of the event 2 arc with the observed plasma flows at THEMIS. A rough comparison of velocities would equate 10 km/s in the ionosphere with 340 km/s in the magnetosphere. On the night of our event, the earthward plasma flows observed by THEMIS are no faster than 200 km/s. The observed motion of the event 2 arc observed in the ionosphere, does not correspond to the magnetospheric plasma flow motion, but it is still within the correct order of magnitude. It is important to keep in mind that this calculation is very approximate and would change greatly depending on the magnetotail configuration.

[38] *Semeter et al.* [2005] present a similar study of the ionospheric signatures of PBIs, using the FAST (Fast Auroral Snapshot Explorer) satellite and the Sondrestrom ISR. The FAST data in the *Semeter et al.* [2005] study cover such a short time span that it is essentially a snapshot in time. The Cascades-2 flight lasts 12 min, allowing us to draw conclusions on the time sequence of events. All streamers

originate at the poleward boundary of the auroral oval, and our event 2 originated from aurora of the type of event 3.

5. Summary and Conclusions

[39] In the community both events 1 and 2 are called inverted-V's but we have shown that they are quite different in their electron distribution functions, with event 1 having only one source population, and event 2 having two separate source populations. The differences in the electron energy distribution functions indicate a different source mechanism for each event. Event 1 fits the definition of an inverted-V, with plasma sheet electrons being weakly accelerated by a parallel potential drop. This type of acceleration mechanism usually happens at altitudes of 2,000-10,000 km. Event 3 fits the definition of Alfvénic aurora, with broad-energy and narrow pitch angle electron distributions [*Paschmann et al.*, 2002]. Event 2 falls somewhere in between, which was similarly found in the study by *Semeter et al.* [2005]. Only with the combination of ground camera data and in situ data can event 2 be categorized as such. Without both parts this arc is easily mistaken for an inverted-V. Event 3 is non-equatorward-extending PBI activity, while event 2 is equatorward-extending PBI activity (a streamer). Event 2 is similar to event 3 in that it includes accelerated ionospheric thermal electrons, with the acceleration zone located at a higher altitude than that of event 3. However, there are no fluctuating DC electric fields observed at the altitude of the rocket during event 2. As all streamers originate at the poleward boundary, as ours is seen in the camera data to do, it can be deduced that the source mechanism for event 2 originated from an event-3-like source at a time before the rocket entered that PBI.

[40] This observation of two PBIs at different stages of their development further solidifies the idea presented by *Hull et al.* [2010], stating that Alfvénic and upward current acceleration regions are not distinct, but rather the latter can develop out of the former. The Cascades-2 case study emphasizes that different auroral acceleration mechanisms, such as quasi-static and Alfvénic, while associated with distinct signatures, are not necessarily occurring separately from one another in space or time. Event 1 and event 3 are clearly shown to be quasi-static and Alfvénic, respectively. Event 2 is found to be a combination of acceleration mechanisms. These observational results are important in illustrating that differing auroral acceleration mechanisms are not always well separated processes, an idea which needs to be incorporated into the theoretical explanation of auroral acceleration.

Appendix A: Bagel Detector

[41] The Bagel detector, Figure A1, is a high resolution, field-aligned electron electrostatic analyzer. It is not a full toroid, but rather, a section of a toroid. The large size of the detector allows for an 8 ms sweep through an energy range of 20 eV to 1 keV. The entrance opening is 2.2 by 0.287 in, mounted on the main payload to sample precipitating, field-aligned electrons.

[42] **Acknowledgments.** The authors wish to thank Larry Lyons (UCLA), Shasha Zou (UMich), Toshi Nishimura (UCLA), Larry Kepko (NASA Goddard), and Bill Lotko (Dartmouth) for useful conversations. The Cascades-2 science team thanks their engineering staff and the personnel at WFF/NSROC, PFRR, and PFISR. The Cascades2 program was funded by the NASA/LCAS program and administered by the WFF/SRPO. D.L. was supported by a subcontract to NASA grant NNX09AI04G to the University of Colorado.

[43] Robert Lysak thanks the reviewers for their assistance in evaluating this paper.

References

Aikio, A. T., K. Mursula, S. Buchert, F. Forme, O. Amm, G. Marklund, M. Dunlop, D. Fontaine, A. Vaivads, and A. Fazakerley (2004), Temporal evolution of two auroral arcs as measured by the Cluster satellite and coordinated ground-based instruments, *Ann. Geophys.*, *22*, 4089–4101.

Aikio, A. T., T. Pitkänen, D. Fontaine, I. Dandouras, O. Amm, A. Kozlovsky, A. Vaivdas, and A. Fazakerley (2008), EISCAT and Cluster observations in the vicinity of the dynamical polar cap boundary, *Ann. Geophys.*, *26*, 87–105.

Angelopoulos, V. (2008), The THEMIS mission, *Space Sci. Rev.*, *141*, 5–34, doi:10.1007/s11214-008-9336-1.

Arnoldy, R., K. Lynch, J. Austin, and P. Kintner (1999), Energy and pitch angle-dispersed auroral electrons suggesting a time-variable, inverted-V potential structure. *J. Geophys. Res.*, *104*(A10), 22613–22621.

Carlson, C. W., D. W. Curtis, G. Paschmann, and W. Michel (1982), An instrument for rapidly measuring plasma distribution functions with high resolution, *Adv. Space Res.*, *2*, 67–70, doi:10.1016/0273-1177(82)90151-X.

Carlson, C. W., et al. (1998), FAST observations in the downward auroral current region: Energetic upgoing electron beams, parallel potential drops, and ion heating, *Geophys. Res. Lett.*, *25*(12), 2017–2020.

Chaston, C. C., L. M. Peticolas, J. W. Bonnell, C. W. Carlson, R. E. Ergun, J. P. McFadden, and R. J. Strangeway (2003), Width and brightness of auroral arcs driven by inertial Alfvén waves, *J. Geophys. Res.*, *108*(A2), 1091, doi:10.1029/2001JA007537.

Chaston, C. C., V. Genot, J. W. Bonnell, C. W. Carlson, J. P. McFadden, R. E. Ergun, R. J. Strangeway, E. J. Lund, and K. J. Hwang (2006), Ionospheric erosion by Alfvén waves, *J. Geophys. Res.*, *111*, A03206, doi:10.1029/2005JA011367.

Davis, T. (1962), The morphology of the auroral displays of 1957–1958: 2. Detail analyses of Alaska data and analyses of high latitude data, *J. Geophys. Res.*, *67*(1), 75–110.

de la Beaujardière, O., L. Lyons, J. Ruohoniemi, E. Friis-Christensen, C. Danielsen, F. Rich, and P. Newell (1994), Quiet-time intensifications along the poleward auroral boundary near midnight, *J. Geophys. Res.*, *99*(A1), 287–298.

Elphinstone, R. D., et al. (1995), The double oval UV auroral distribution: 1. Implications for the mapping of auroral arcs, *J. Geophys. Res.*, *100*(A7), 12075–12092.

Evans, D. (1974), Precipitating electron fluxes formed by a magnetic field aligned potential difference, *J. Geophys. Res.*, *79*(19), 2853–2858.

Frederick-Frost, K. M., K. A. Lynch, P. M. Kintner Jr., E. Klatt, D. Lorentzen, J. Moen, Y. Ogawa, and M. Widholm (2007), SERSIO: Svalbard EISCAT rocket study of ion outflows, *J. Geophys. Res.*, *112*, A08307, doi:10.1029/2006JA011942.

Hasegawa, A. (1976), Particle acceleration by MHD surface wave and formation of aurora, *J. Geophys. Res.*, *81*(28), 5083–5090.

Heinselman, C. J., and M. J. Nicolls (2008), A Bayesian approach to electric field and *E*-region neutral wind estimation with the Poker Flat Advanced Modular Incoherent Scatter Radar, *Radio Sci.*, *43*, RS5013, doi:10.1029/2007RS003805.

Henderson, M. G., G. D. Reeves, and J. S. Murphree (1998), Are north–south aligned auroral structures an ionospheric manifestation of bursty bulk flows?, *Geophys. Res. Lett.*, *25*(19), 3737–3740.

Hull, A. J., M. Wilber, C. C. Chaston, J. W. Bonnell, J. P. McFadden, F. S. Mozer, M. Fillingim, and M. L. Goldstein (2010), Time development of field-aligned currents, potential drops, and plasma associated with an auroral poleward boundary intensification, *J. Geophys. Res.*, *115*, A06211, doi:10.1029/2009JA014651.

Ivchenko, N., E. M. Blixt, and B. S. Lanchester (2005), Multispectral observations of auroral rays and curls, *Geophys. Res. Lett.*, *32*, L18106, doi:10.1029/2005GL022650.

Keiling, A., K.-H. Kim, J. R. Wygant, C. Cattell, C. T. Russell, and C. A. Kletzing (2003), Electrodynamics of a substorm-related field line resonance observed by the Polar satellite in comparison with ground Pi2 pulsations, *J. Geophys. Res.*, *108*(A7), 1275, doi:10.1029/2002JA009340.

Keiling, A., et al. (2008), Multiple intensifications inside the auroral bulge and their association with plasma sheet activities, *J. Geophys. Res.*, *113*, A12216, doi:10.1029/2008JA013383.

Kepko, L., E. Spanswick, V. Angelopoulos, E. Donovan, J. McFadden, K. H. Glassmeier, J. Raeder, and H. J. Singer (2009), Equatorward

moving auroral signatures of a flow burst observed prior to auroral onset, *Geophys. Res. Lett.*, *36*, L24104, doi:10.1029/2009GL041476.

Lui, A. T. Y. (2001), Current controversies in magnetospheric physics, *Rev. Geophys.*, *39*(4), 535–563, doi:10.1029/2000RG000090.

Lummerzheim, D., and J. Lilensten (1994), Electron transport and energy degradation in the ionosphere: Evaluation of the numerical solution, comparison with laboratory experiments and auroral observations, *Ann. Geophys.*, *12*, 1039–1050.

Lynch, K. A., R. L. Arnoldy, P. M. Kintner, and J. Bonnell (1996), The AMICIST auroral sounding rocket: A comparison of transverse ion acceleration mechanisms, *Geophys. Res. Lett.*, *23*(23), 3293–3296.

Lyons, L., T. Nagai, G. Blanchard, J. Samson, T. Yamamoto, T. Mukai, A. Nishida, and S. Kokubun (1999), Association between GEOTAIL plasma flows and auroral poleward boundary intensifications observed by CANOPUS photometers, *J. Geophys. Res.*, *104*, 4485–4500.

Lyons, L. R., E. Zesta, Y. Xu, E. R. Sánchez, J. C. Samson, G. D. Reeves, J. M. Ruohoniemi, and J. B. Sigwarth (2002), Auroral poleward boundary intensifications and tail bursty flows: A manifestation of a large-scale ULF oscillation, *J. Geophys. Res.*, *107*(A11), 1352, doi:10.1029/2001JA000242.

Lysak, R. L., Y. Song, and T. W. Jones (2009), Propagation of Alfvén waves in the magnetotail during substorms, *Ann. Geophys.*, *27*, 2237–2246, doi:10.5194/angeo-27-2237-2009.

Marklund, G. T., et al. (2001), Temporal evolution of the electric field accelerating electrons away from the auroral ionosphere, *Nature*, *414*, 724–727.

Marklund, G. T., et al. (2004), Characteristics of quasi-static potential structures observed in the auroral return current region by Cluster, *Nonlinear Processes Geophys.*, *11*, 709–720.

McFadden, J., C. Carlson, R. Ergun, D. Klumpar, and E. Moebius (1999). Ion and electron characteristics in auroral density cavities associated with ion beams: No evidence for cold ionospheric plasma. *J. Geophys. Res.*, *104*(A2), 14,671–14,682.

Nicolls, M. J., and C. J. Heinselman (2007), Three-dimensional measurements of traveling ionospheric disturbances with the Poker Flat Incoherent Scatter Radar, *Geophys. Res. Lett.*, *34*, L21104, doi:10.1029/2007GL031506.

Olsson, A., and P. Janhunen (1998), A case study of electron precipitation in the late substorm growth phase on and nearby a preonset arc, *Ann. Geophys.*, *16*, 1567–1572.

Paschmann, G., S. Haaland, and R. Treumann (Eds.) (2002), *Auroral Plasma Physics*, Kluwer Acad., Dordrecht, Netherlands.

Persoon, A., D. Gurnett, W. Peterson, J. Waite Jr., J. Burch, and J. L. Green (1988), Electron density depletions in the nightside auroral zone, *J. Geophys. Res.*, *93*(A3), 1871-1895.

Robinson, R. M., and R. R. Vondrak (1985), Characteristics and sources of ionization in the continuous aurora, *Radio Sci.*, *20*, 447–455.

Semeter, J., C. J. Heinselman, G. G. Sivjee, H. U. Frey, and J. W. Bonnell (2005), Ionospheric response to wave-accelerated electrons at the poleward auroral boundary, *J. Geophys. Res.*, *110*, A11310, doi: 10.1029/2005JA011226.

Streltsov, A. V., and W. Lotko (2008), Coupling between density structures, electromagnetic waves and ionospheric feedback in the auroral zone, *J. Geophys. Res.*, *113*, A05212, doi:10.1029/2007JA012594.

Tsyganenko, N. A., and M. I. Sitnov (2005), Modeling the dynamics of the inner magnetosphere during strong geomagnetic storms, *J. Geophys. Res.*, *110*, A03208, doi:10.1029/2004JA010798.

Watt, C. E. J., R. Rankin, and R. Marchand (2004), Kinetic simulations of electron response to shear Alfven waves in magnetospheric plasmas, *Phys. Plasmas*, *11*, 1277–1284.

Wygant, J., et al. (2000), Polar spacecraft based comparisons of intense electric fields and Poynting flux near and within the plasma sheet-tail lobe boundary to UVI images: An energy source for the aurora, *J. Geophys. Res.*, *105*(A8), 18675–18,692.

Wygant, J. R., et al. (2002), Evidence for kinetic Alfvén waves and parallel electron energization at 4–6 R_E altitudes in the plasma sheet boundary layer, *J. Geophys. Res.*, *107*(A8), 1201, doi:10.1029/2001JA900113.

Zesta, E., L. Lyons, C. P. Wang, E. Donovan, H. Frey, and T. Nagai (2006), Auroral poleward boundary intensifications (PBIs): Their two-dimensional structure and associated dynamics in the plasma sheet, *J. Geophys. Res.*, *111*, A05201, doi:10.1029/2004JA010640.

Zou, S., L. R. Lyons, M. J. Nicolls, C. J. Heinselman, and S. B. Mende (2009), Nightside ionospheric electrodynamics associated with substorms: PFISR and THEMIS ASI observations, *J. Geophys. Res.*, *114*, A12301, doi:10.1029/2009JA014259.

H. Dahlgren, Center for Space Physics, Boston University, 725 Commonwealth Ave., Boston, MA 02215, USA. (hannad@kth.se)

D. L. Hampton, D. Lummerzheim, and H. C. Stenbaek-Nielsen, Geophysical Institute, University of Alaska Fairbanks, Fairbanks, AK 99775-7320, USA. (dhampton@gi.alaska.edu; lumm@gi.alaska.edu; hans.nielsen@gi.alaska.edu)

P. M. Kintner and E. T. Lundberg, School of Electrical and Computer Engineering, Cornell University, Rhodes Hall 301, Ithaca, NY 14850, USA. (pmk1@cornell.edu; etl22@cornell.edu)

M. Lessard, Space Science Center, University of New Hampshire, Durham, NH 03824, USA. (marc.lessard@unh.edu)

K. A. Lynch and M. R. Mella, Department of Physics and Astronomy, Dartmouth College, 6127 Wilder Laboratory, Hanover, NH 03755, USA. (kristina.a.lynch@dartmouth.edu; meghan.r.mella@dartmouth.edu)

M. J. Nicolls, Center for Geospace Studies, SRI International, Menlo Park, CA 94025, USA. (michael.nicolls@sri.com)